Deep shear wave velocity profiles of the Santiago Basin for evaluation of seismic response

Conference Paper · September 2017

5 authors, including:

Cesar Pasten
University of Chile
50 PUBLICATIONS   **322** CITATIONS

SEE PROFILE

José Salomón
University of Chile
5 PUBLICATIONS   **22** CITATIONS

SEE PROFILE

Miguel Saez
University of Chile
9 PUBLICATIONS   **23** CITATIONS

SEE PROFILE

Sergio Ruiz
University of Chile
94 PUBLICATIONS   **695** CITATIONS

SEE PROFILE

Some of the authors of this publication are also working on these related projects:

Seismic Response in Subduction Environments View project

Site Effects Observatory on an Alluvial Basin View project

Deep shear wave velocity profiles of the Santiago Basin for evaluation of seismic response

Profils profonds de la vitesse des ondes de cisaillement du bassin de Santiago pour l'évaluation de la réponse sismique

César Pastén, José Salomón, Miguel Sáez
Department of Civil Engineering, University of Chile, Chile, cpasten@ing.uchile.cl

Sergio Ruiz
Department of Geophysics, University of Chile, Santiago, Chile

Felipe Leyton
National Seismological Center, University of Chile, Santiago, Chile

ABSTRACT: Evaluation of the seismic response of the Santiago Basin requires a shear wave velocity model with vertical and lateral variations that may explain the site effects reported during the 2010 Maule Earthquake. In order to investigate the velocity structure of the Basin, we used a temporal broadband station network that continuously recorded months of ambient seismic noise and cross-correlated the vertical components of the records. Identification of zero-crossings in the real part of the cross spectrum between stations were associated with the zeros of the zero-order Bessel function to obtain phase-velocity dispersion curves. These curves were combined using a least-squares inversion to obtain phase velocity maps for periods ranging between 0.8s and 5s. The spatial distribution of the temporal broadband network was complemented with a permanent accelerometer network that allows imaging longer periods associated to the deeper Basin structure and a smaller portable geophones network that allows defining shorter periods dominated by the shallower soil deposits. The phase velocity maps were used to generate a 1D shear wave velocity profiles using the Neighborhood algorithm. The profiles resolve changes in velocity up to 3 km depth and predict velocities that rapidly reach 1 km/s at relatively shallow depths.

RESUMÉ: L'évaluation de la réponse sismique du bassin de Santiago requiert l'utilisation d'un modèle de Vs à variations verticales et horizontales afin d'expliquer les effets de site reportés après le tremblement de terre du Maule 2010. Afin de rechercher la structure de vitesse du bassin, nous avons utilisé un réseau temporel de stations large bande, lequel enregistra de façon continue plusieurs mois de bruit sismique ambiant. Nous avons comparé les composantes verticales des registres. Les zéros de la partie réelle du spectre de corrélation furent associés aux zéros d'une fonction de Bessel d'ordre zéro afin d'obtenir des courbes de dispersión. Ces courbes furent combinées en utilisant une inversion des moindres carrés dans le but d'obtenir des cartes de vitesses de phase à diverses périodes. La couverture fournie par les stations à large bande fut complétée par un réseau d'accéléromètres permettant de couvrir des hautes périodes ainsi que des géophones portables afin de couvrir les périodes basses caractéristique des dépôts de sols superficiels. Les cartes de vitesse ont permis de générer des profils 1D de Vs en utilisant l'algorithme de Quartier. Ces profils permettent la résolution de changements de vitesse jusqu'à une profondeur de 3 km et atteignent rapidement 1 km/s à faible profondeur.

KEYWORDS: Cross-correlation, Ambient noise tomography, shear wave velocity.

1 INTRODUCTION

The shear wave velocity of the sediments, the velocity contrasts between the bedrock and the soil, and the geomorphology of a sedimentary basin are the main parameters that control the amplification of seismic waves during earthquakes (Fäh et al. 2003). This suggests the importance of measuring soil properties at considerable depths. In the case of the Santiago Basin, an available gravimetric model shows a basement with a mean depth of 250 meters and the presence of two depocenters reaching 500 m depth (Yañez et al.2015).

During the last decades, the seismic prospecting surface wave methods have been widely used to characterize the seismic behavior of soil profiles through the determination of shear wave velocities (Xia et al. 1999). Although the surface wave methods, whether active or passive, are non-invasive and cheaper than traditional prospecting methods, they are limited to around 100 m depth (Horike 1985) mainly due to the maximum distance between receivers, associated to the maximum observable wavelength, and the energy of the source.

In this study, we propose a methodology to estimate deep shear wave velocity profiles that will allow us to understand the seismic response of the Santiago Basin. To this aim, we used a temporal broadband station network that continuously recorded months of ambient seismic noise and extracted dispersive information from the deep sediment layers using a technique known as ambient noise tomography (Bensen et al. 2009, Yang et al. 2007). The methodology determines dispersion curves using the spectral method proposed by Pasten et al. (2016) and the generation of phase velocity maps at different frequencies using a regularized least squares inversion scheme. These maps are complemented with local measurements to calculate dispersion curves over a wide range of frequencies. The dispersion curves are inverted using the Neighborhood algorithm (Sambridge 1999) to obtain deep shear wave velocity profiles for different zones of the basin.

2 SEISMIC NETWORKS AND DATA PROCESSING

In this study, we used data from a temporary seismic network deployed over the Santiago basin that recorded months of ambient seismic noise during 2013 and 2014 (Figure 1). The seismic array consisted of 29 broadband Nanometrics Trillium Compact 120s sensors. Data from this network was complemented with continuous records from 12 Kinemetrics Basalt sensors that belong to the Accelerometric National Chilean Network.

We detemined the cross-correlation of two vertical records following the spectral methodology proposed by Pastén et al. (2016), which comprises the next steps:

1. The instrumental response was removed from the raw data following Tibuelac et al. (2011)
2. The records were high-pass filtered with a 4th-order Butterworth filter (0.01 Hz cutoff frequency), and divided in 2 minutes windows.
3. The cross-correlation was calculated in each window, the real component was normalized by its maximum absolute value and daily stacked.
4. The spectra from all available days were stacked generating a final spectrum. Then, zero-crossings were identified and associated to the zero-crossings of a Bessel function of the first kind (J_o).
5. The phase velocity $c(f_n)$ was calculated from the interstation distance Δ, and the value of the zero-crossing frequency of the Bessel function z_{n+m} as (Ekström 2009):

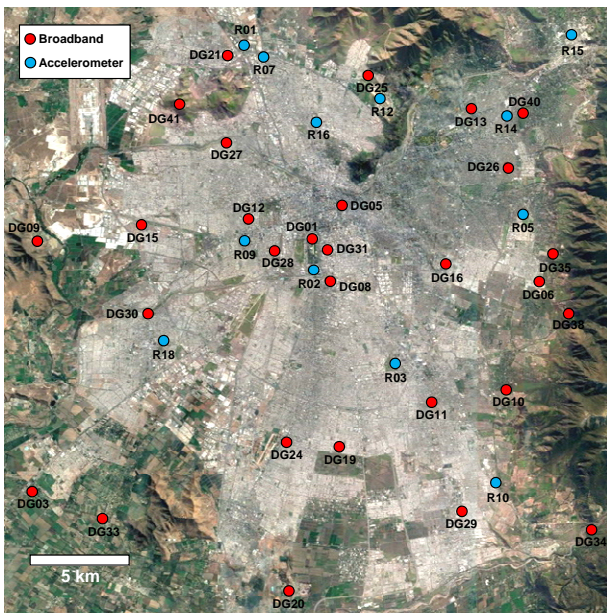$$c(f_n) = \frac{2\pi f_n \Delta}{z_{n+m}} \qquad (1)$$

Figure 1. Stations network in the Santiago Basin.

Using all the available station pairs, we calculated more than 500 cross-correlations and applied a selection criterion in order to identify the maximum valid frequency for each dispersion curve. The criterion is based on the stability of the daily spectrum at each frequency and includes three steps. First, we normalized the daily spectrum using a one-bit normalization. Then, the amplitudes were stacked generating the "one-bit" final spectrum, which was smoothed over a 0.2 Hz bandwidth. Finally, we calculated the standard deviation at each frequency. If the daily spectrum at a given frequency was stable, the standard deviation approaches zero. We found that frequencies with standard deviations lower than 0.8 are associated to zero-crossings that can be clearly identified. The Figure 2 shows a summary of all the successfully calculated dispersion curves.

Once all the dispersion curves were determined, an observed traveltime t_{obs} was calculated to each pair of stations, dividing the interstation distance by the calculated phase velocity at certain frequency.
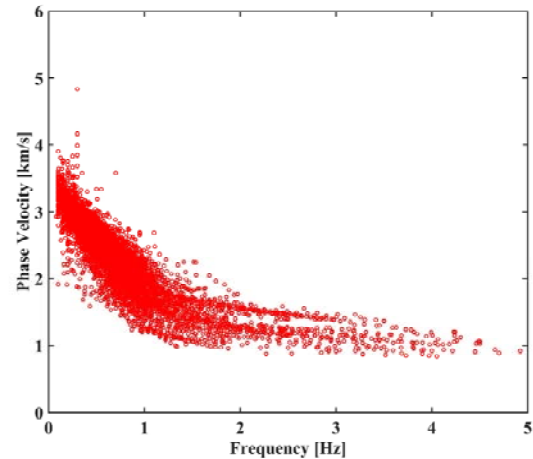

Figure 2. Calculated phase velocity dispersion curves (529 in total).

3 TRAVELTIME TOMOGRAPHY

3.1 Inversion Scheme

The traveltime t for a ray passing between two stations can be expressed as the integral of the slowness field (inverse of velocity) through the path geometry at certain frequency. The problem of deriving the velocity field from a number of measurements at the surface is highly nonlinear due to the dependency of the ray path geometry and the media structure (Nolet 2012). However, given the error levels associated to the data from shallow surveys, a linear approximation based on straight ray paths is sufficient to estimate the slowness model (Kugler et al. 2007, Picozzi et al. 2009). Then, assuming straight rays and discretizing the slowness field in a 2D array of M pixels, the traveltime forward problem can be written as:

$$\underline{t} = \underline{\underline{G}}\,\underline{s} \qquad (2)$$

Where $\underline{t}$ is the traveltime vector [Nx1], $\underline{s}$ is the slowness vector [Mx1] and $\underline{\underline{G}}$ is the design matrix [NxM], where each column is associated to the length of the ray that passes through the corresponding pixel.

Generally, the Eq. 2 cannot be solved directly because the data kernel $\underline{\underline{G}}$ is not invertible. Furthermore, most tomographic problems can be considered as mixed determined (Menke 2012), so the solution requires a priori information about the estimated model. Then, the slowness field is found by minimizing the L2 norm between the observed $\underline{t}_{obs}$ and the predicted traveltimes vector $\underline{t}$, including a Laplacian operator and a homogeneous initial model $\underline{s}_o$. The misfit function is:

$$\varphi(\underline{s}) = (\underline{t} - \underline{\underline{G}}\underline{s})^T W(\underline{t} - \underline{\underline{G}}\underline{s}) + \varepsilon^2 \left(\nabla^2 (\underline{s} - \underline{s}_o) \right) \qquad (3)$$

Where ε^2 is the damping parameter and W is the Cholesky decomposition of the variance matrix. The optimal value of ε^2 is estimated using the generalized cross validation method (Craven & Wahba 1978). The initial model $\underline{s}_o$ considers a constant slowness value estimated from the average phase velocity value at certain frequency.

3.2 Data Validation and Model Discretization

The size of the pixels and the resolution of the 2D slowness field is constrained by the larger wavelength observed at each frequency. The quarter-wavelength criterion has been used by several authors as the model resolution limit (Long and Kocaoglu 2001), and establishes that the deviation of the wave paths from a straight line in media with slight velocity

anomalies is either in the same order of magnitude of the pixels dimension or less than a quarter of the wavelength (Pilz et.al 2012). Then, as an average, the model is discretized into a grid of 2x2 km^2 pixels, covering an area of 32x30 km^2.

In order to evaluate the quality of the ray path coverage and to verify its capability to recover velocity contrasts, we generated a checkerboard test with a synthetic velocity model. The model followed a checkerboard pattern with a velocity contrast of a 100% between pixels. The checkerboard was used to generate synthetic observed traveltimes that were disturbed by adding a Gaussian noise (zero mean and 5% variance). Then, the synthetic data was inverted using the scheme described in the previous section. As a result, the synthetic model suggests that the ray coverage could be appropriate to recover the real velocity model over a frequency range between the 0.2 Hz and 1.2 Hz.

3 .3 *Phase Velocity Maps*

Applying the inversion procedure described above to the measured data, we obtained the phase velocity maps shown in Figure 3. The results are expressed in terms of the perturbation percentage with respect to the average map velocity value c_{mean}. Note that the pixels that are not crossed by any ray are painted in gray and the black dots indicate the stations positions in Figure 1.

The results show a homogeneous velocity distribution at lower frequencies (Figure 3a) and an increasing heterogeneity at higher frequencies (Figure 3c y Figure 3d), reaching velocity perturbations as high as 30%. Also, the maps show that the south of the basin has larger phase velocities compared to the north zone, which is consistent with Pastén et al. (2016). The high velocity zones at higher frequencies shown in Figure 3d are in good agreement with the main rock outcrops of the basin.

4 SHEAR WAVE VELOCITY PROFILES

In order to generate dispersion curves over a wider range of frequencies, we performed three local scale experiments in the center, the east and the south of the basin (shown in the Figure 3a). We used four portable 4.5 Hz geophones (Tromino®) set to a sampling frequency of 128 Hz. The devices were arranged in quadrilateral configurations with inter-sensor distances between 20 m and 100 m. We calculated the phase velocity for each pair of geophones by applying the spectral methodology described above to 50 min ambient noise records.

The final dispersion curves were obtained by coupling the reconstructed curves from the corresponding pixel in the phase velocity maps (Figure 3) and the local dispersion measurements. We complemented the intermediate frequency range using three pair of broadband stations: DG28-DG31 in the south, DG06-DG26 in the east and DG19-DG24 in the center of the basin. The curves displayed in Figure 4a show that the tomographic results are in good agreement with the local dispersion curves. This fit validates the use of the ambient noise tomography as complementary information to improve the definition of local dispersion curves at lower frequencies.

The resulting dispersion curves were inverted to obtain shear wave velocity profiles using the Geopsy software (www.geopsy.org). The inversion was realized based on Monte Carlo simulations with 500,000 runs. Given the steady decrease of the phase velocity with frequency, we assumed that the shear wave velocity increases with depth following a power law. The inverted shear wave velocity profiles are shown in Figure 4 and indicate that the Vs values rapidly vary between 0.3 and 3.4 km/s in the East sector (Figure 4b), between 0.4 and 3.5 km/s in the Center zone (Figure 4d), and between 0.5 and 3.5 km/s in the South zone (Figure 4c). These results are consistent with the calculated dispersion curves and the Vs values for the surface geology of the basin (Leyton et al. 2011).
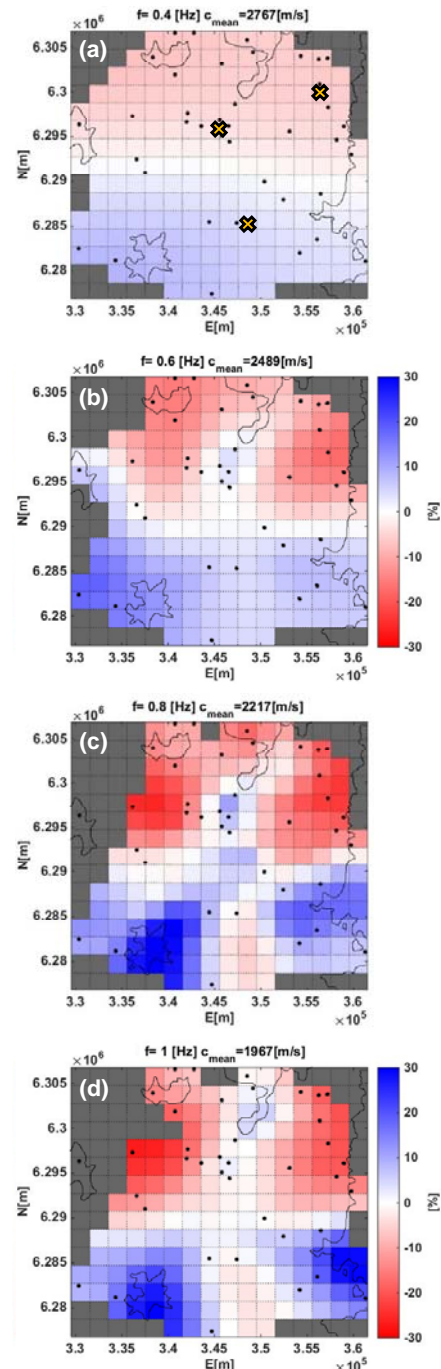

Figure 3. Phase velocity maps at (a) 0.2 Hz, (b) 0.6 Hz, (c) 0.8 Hz, and (d) 1.0 Hz. The locations of the local experiments are represented by a X symbol in panel (a).

5 CONCLUSIONS AND FINAL COMMENTS

In this work, we report the use of an accelerometric network and a temporal broadband station network that continuously recorded months of ambient seismic noise to cross-correlate the vertical components of the records and to calculate over 500 dispersion curves using the real component of the cross spectra. This methodology allowed generating phase velocity maps at low frequencies in the range between 0.2 and 1.2 Hz. These maps were complemented with local ambient noise measurements in order to obtain dispersion curves along a wider range of frequencies (0.2 Hz-20 Hz). The dispersion curves were inverted to generate deep shear wave velocity profiles in three zones of the basin. The velocities increase

rapidly with depth to reach values as high as 1 km/s at less than 200 m.
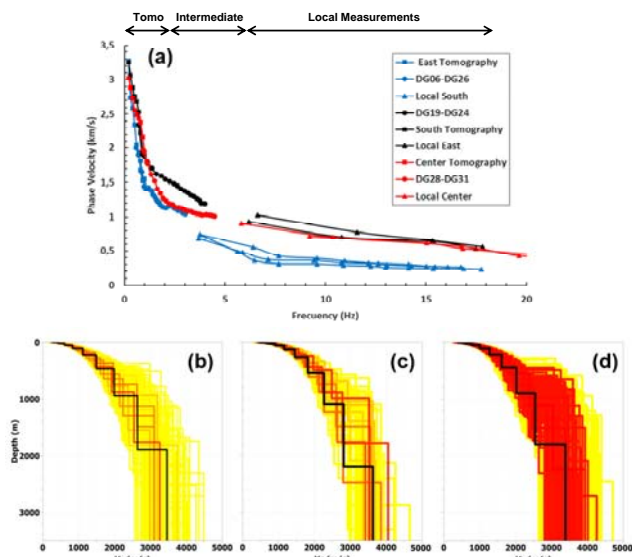

Figure 4. (a) Dispersion curves over a wide range of frequencies. Shear wave velocity profiles for (b) the East, (c) the South, and (d) the Center zone. The shown Vs profiles are the best 1,000 profiles that have the lowest misfit with respect to the measured dispersion curve.

The ambient noise tomography can be used to detect velocity anomalies with depth, even at a geotechnical scale. The resolution of the velocity model depends on the availability of data and the solved range of frequencies, or the observable wavelengths. In order to improve the spatial resolution and the range of frequencies of the model, we suggest to complement the available data with temporal broadband stations focusing on low ray density areas, including short and intermediate distances between receivers (< 4 km).

6 ACKNOWLEDGEMENTS

7 REFERENCES

Xia, J., Miller, R. D., & Park, C. B. 1999. Estimation of near-surface shear-wave velocity by inversion of Rayleigh waves. *Geophysics,* 64(3), 691-700.

Fäh, D., Kind, F., & Giardini, D. 2003. Inversion of local S-wave velocity structures from average H/V ratios, and their use for the estimation of site-effects. *Journal of Seismology*, 7(4), 449-467.

Yáñez, G., Muñoz, M., Flores-Aqueveque, V., & Bosch, A. 2015. Gravity derived depth to basement in Santiago Basin, Chile: implications for its geological evolution, hydrogeology, low enthalpy geothermal, soil characterization and geo-hazards. *Andean Geology*, 42(2), 147-172.

Horike, M. 1985 Inversion of phase velocity of long-period microtremors to the S-wave-velocity structure down to the basement in urbanized areas. *Journal of Physics of the Earth*, 33(2), 59-96.

Bensen, G. D., Ritzwoller, M. H., & Yang, Y. 2009. A 3-D shear velocity model of the crust and uppermost mantle beneath the United States from ambient seismic noise. *Geophysical Journal International*, 177(3), 1177-1196.

Yang, Y., Ritzwoller, M. H., Levshin, A. L., & Shapiro, N. M. 2007. Ambient noise Rayleigh wave tomography across Europe. *Geophysical Journal International*, 168(1), 259-274.

Pastén, C., Sáez, M., Ruiz, S., Leyton, F., Salomón, J., & Poli, P. 2016. Deep characterization of the Santiago Basin using HVSR and cross-correlation of ambient seismic noise. *Engineering Geology*, 201, 57-66.

Sambridge, M. 1999. Geophysical inversion with a neighbourhood algorithm—II. Appraising the ensemble. *Geophysical Journal International*, 138(3), 727-746.

Tibuleac, I. M., Von Seggern, D. H., Anderson, J. G., & Louie, J. N. 2011. Computing Green's functions from ambient noise recorded by accelerometers and analog, broadband, and narrow-band seismometers. *Seismological Research Letters*, 82(5), 661-675.

Ekström, G., Abers, G. A., & Webb, S. C. 2009. Determination of surface-wave phase velocities across USArray from noise and Aki's spectral formulation. *Geophysical Research Letters*, 36(18).

Nolet, G. (Ed.). 2012. Seismic tomography: with applications in global seismology and exploration geophysics (Vol. 5). *Springer Science & Business Media*.

Picozzi, M., Parolai, S., Bindi, D., & Strollo, A. 2009. Characterization of shallow geology by high-frequency seismic noise tomography. *Geophysical Journal International*, 176(1), 164-174.

Menke, W. 2012. Geophysical data analysis: Discrete inverse theory (Vol. 45). *Academic press*.

Craven, P., & Wahba, G. 1978. Smoothing noisy data with spline functions. *Numerische Mathematik*, 31(4), 377-403.

Long, L. T., & Kocaoglu, A. H. 2001. Surface-wave group-velocity tomography for shallow structures. *Journal of Environmental & Engineering Geophysics*, 6(2), 71-81.

Pilz, M., Parolai, S., Picozzi, M., & Bindi, D. 2012. Three-dimensional shear wave velocity imaging by ambient seismic noise tomography. *Geophysical Journal International*, 189(1), 501-512.

Panza, G. F. 1981. The resolving power of seismic surface waves with respect to crust and upper mantle structural models. In The solution of the inverse problem in geophysical interpretation *Springer US*. 39-77.

Leyton, F., Sepúlveda, S. A., Astroza, M., Rebolledo, S., Acevedo, P., Ruiz, S., & Foncea, C. 2011. Seismic zonation of the Santiago basin, Chile. *In 5th International Conference on Earthquake Geotechnical Engineering*.